JOHNSON MATTHEY
TECHNOLOGY REVIEW

Towards 3D-Electrical Capacitance Tomography for Interface Detection

Thresholding method improves accuracy for real-world 3D process monitoring

Peter J. Clark* and Giuseppe Forte

Johnson Matthey Technology Centre, Billingham, UK, TS23 1LB; and School of Chemical Engineering, University of Birmingham, Edgbaston, UK, B15 2TT

*Email: peter.clark@matthey.com

Mark J. H. Simmons

School of Chemical Engineering, University of Birmingham, Edgbaston, UK, B15 2TT

E. Hugh Stitt

Johnson Matthey Technology Centre, Billingham, UK, TS23 1LB

The application of three-dimensional electrical capacitance tomography (3D-ECT) for the *in situ* monitoring of a hard boundary or interface has been investigated using imaged phantoms that simulate real-life processes. A cylinder-in-tube phantom manufactured from polyethylene (PE), a low di-electric and non-conductive material, was imaged using the linear back projection (LBP) algorithm with the larger tube immersed at varying intervals to test the ability of the technique to image interfaces axially through the sensor. The interface between PE and air is clearly imaged and correlates to the known tube penetration within the sensor. The cylinder phantom is imaged in the centre of the sensor; however, the reduction in measurement density towards the centre of the ECT sensor results in reduced accuracy. A thresholding method, previously applied to binary systems to improve the imaged accuracy of a hard boundary between two separate phases, has been applied to the 3D-ECT tomograms that represent the PE phantom. This approach has been shown to improve the accuracy of the acquired image of a cylinder of air within a non-conductive PE tube.

1 Introduction

The ability to accurately and quickly monitor the evolution of physical and chemical changes within products during manufacturing has been the subject of much interest in both academic and industrial research communities. Enhanced process monitoring allows an engineer to implement better control thereby increasing efficiency, improving material and energy usage and increasing product quality. Electrical tomography has been developed over the last few decades with the purpose of delivering real time, *in situ* measurements of phase distributions within a process vessel or pipe. It provides spatially resolved information on the distribution of material properties (permittivity, conductivity, density) within a cross-sectional plane through the sensing zone represented by a pixel grid known as a tomogram. In the majority of cases to date two-dimensional (2D) images have been sufficient to provide the required process information for the user;

however, 3D tomography provides spatial information in both radial and axial planes yielding greater process insight. The compromise when applying 3D methods as opposed to 2D is increased computing time, greater complexity of hardware and requirement for advanced reconstruction algorithms.

Electrical tomography is categorised as a 'soft-field' method. The distribution of the electric field within the sensor is unknown thus forming a non-linear relationship between the measured capacitances at the boundary of the sensor and the material distribution within the sensor. ECT is a specific form of electrical tomography applicable to systems with a non-conductive continuum and an insulating process vessel wall. It utilises a concentric ring of uniformly spaced electrodes fixed to the outside of a non-conductive vessel wall. The signal-to-noise ratio (SNR) of the system is dependent upon the area of each electrode therefore studies have been conducted that determine the optimal size of ECT electrodes (1). Guard electrodes are also required to prevent process materials outside the sensing zone having an effect upon the electric field distribution (2). The number of electrodes used within the sensor ring is a compromise between the required size of electrode to deliver the required SNR, the diameter of the electrode array (directly related to the diameter of the process vessel) and the desired reconstructed image accuracy, with a greater number of electrodes delivering increased spatial resolution.

There are two critical parameters when designing an ECT sensor: the ratio of permittivity of continuous and dispersed phases and the thickness of the sensor liner (3). When either of these phases has a high relative permittivity there is an increased electrical flux deflection at the boundary of the ECT sensor that results in the relationship between material permittivity and measured capacitance becoming non-linear, typically at relative permittivity values $\varepsilon_{mat} > 15$. To image these materials a new sensor was developed that applies internal rather than external electrodes to measure the boundary inter-electrode capacitance. This system has been used to image an air/de-mineralised water phantom and a water continuous oil-in-water dispersion designed to mimic process equipment in the oil industry such as separators and extraction units (3). Whilst the configuration of the sensor solves the boundary linearity problem, it removes the non-intrusive advantage that traditional ECT has over competing methods. In the majority of the process industries it is unlikely that a pipe or unit will be taken offline for electrode fitting, and

indeed due to the hazardous nature of the chemicals used any potential for containment risk is unacceptable.

Liquid hold up within a gas/liquid packed bed has been investigated using twin-plane ECT for application within chemical reactors. Initial measurements using single plane ECT were conducted to determine liquid drainage dynamics and determine their relationship with the gas velocity and packing particle size. Extensive calibrations were performed using twin plane ECT so as to accurately map bed hydrodynamics across the dual sensing zones and the use of tracer led residence time distribution (RTD) combined with ECT analysis to obtain hydrodynamic performance data was also investigated (4).

Image refinement of 2D tomograms of high dielectric materials using commercially available ECT equipment has previously been addressed by the present authors (5, 6). The focus of that study was to vary the threshold value and optimise the image based upon image error as a function of the threshold. Two known methods for determining image error were compared: pixel-by-pixel (PbP) (Equation (i)) and areal (Equations (ii) and (iii)):

$$e_{PbP} = \frac{100}{N} \sum_{i=1}^{N} \frac{|(\mu_{image} - \mu_{real})|}{\mu_{real}} \qquad \text{(i)}$$

where e_{PbP} is the error using the PbP approach, N is the total number of pixels, μ_{image} is the imaged pixel value of pixel i in the tomogram and μ_{real} is the theoretical pixel value of pixel i in the real system. The areal analysis is given as two stages; the first calculates the area of the image occupied by the phantom:

$$A_{image} = A_C \frac{\sum \mu_{image}}{N} \Big|_{\mu_{image<t}} \qquad \text{(ii)}$$

where A_{image} is the area of the image and A_C is the cross-sectional area of the circular sensor chamber. The second stage calculates the error as a ratio of the difference between the areas of the imaged and real object to the area of the real object:

$$e_A = \frac{|A_{image} - A_{phantom}|}{A_{phantom}} \qquad \text{(iii)}$$

where e_A is the image error calculated using the areal approach and $A_{phantom}$ is the area of the phantom. These two methods were compared to determine the sensitivity of image error to threshold value. The

important conclusions were: (a) the optimal threshold values calculated using each method are consistent, demonstrating robustness; and (b) the calculated image error using the areal approach is much lower as it is not constrained to the pixel resolution.

A similar study was conducted with the aim of defining 'limited region tomography' (7, 8). This is a method based upon defining a region to which the reconstruction is applied using a narrowband pass filter. The accuracy of the image is increased by limiting the image area, thereby reducing the number of unknown pixels and enhancing the resolution. This approach has so far been applied predominantly for detection of deposits and scaling in pipes, although the potential applications stretch to any purpose whereby imaging of the whole tomographic plane is not essential. However, this method is currently not a commercially available technology.

The definitions of 3D and 'pseudo-3D' tomography are confusing and often misapplied in the existing literature on this subject. Until recently there was a lack of precision hardware and capable software that could obtain full 3D-ECT data, that is to say acquire and reconstruct electrode measurements in the axial, radial and angular dimensions (assuming cylindrical coordinates). Prior to suitable commercial equipment being available, 2D tomograms were stacked to obtain 'pseudo-3D' images of a process. The term 'pseudo' is used as there are no electrode measurements across the axial plane (9).

An electrical capacitance volume tomography (ECVT) approach has been used to monitor the hydrodynamics of the drying of wet granules with the purpose of being used in the pharmaceutical industry. From the 3D data gained the granule moisture content and drying medium velocity were calculated (10).

The majority of work so far in applied 3D-ECT research has used back-projection approaches for simplicity, however there has been some work done on a volumetric 3D approach using alternative reconstruction algorithms. A neural-network multi-criterion optimisation image reconstruction technique (NN-MOIRT) algorithm has been developed that effectively applies the optimisation approach across a Hopfield neural network (11). The results have been compared favourably with existing reconstruction algorithms such as the iterative filtered back projection technique (IFBPT) and the iterative linear back projection (ILBP) algorithm. The NN-MOIRT algorithm was then applied to a three phase bubble column so as to image multi-phase flows and showed the enhanced

accuracy of this method for 3D-ECT applications (12). The same group then used this approach to investigate the dynamics of spiral bubble plume motion in the entrance zone of bubble columns and three-phase fluidised beds (13). The NN-MOIRT approach was again combined with volumetric ECT to investigate a jet of air, issued from a single orifice, within a poppy seed bed of internal diameter 50 mm. The ECVT results were thresholded to yield optimal images and then compared directly with magnetic resonance imaging (MRI) data showing consistency at high air flow rates, although the ECVT was less sensitive than MRI to changes at lower air flow. Standard deviation measurements across the ECVT images gave 7 mm in the radial plane and 8 mm in the axial plane, at least an order of magnitude higher than MRI. From this it may be concluded that significant further improvement is required for ECT to be considered an accurate imaging technique (14).

In another study, moving objects were imaged using 3D-ECT. Images of a rod and a ball were separately moved down the central axis and periphery of the sensor (15). A Gauss-Newton reconstruction algorithm was used, another approach that is not yet commercially available and is largely confined to academia, yielding an image error of approximately 10% although this increased by 2% when the imaged objects were at the sensor periphery. Interestingly, a parallel study was conducted that arrived at the same conclusion in that the image error at the wall was greater than in the centre of sensor. The reasoning for this observation is that the incidence of convergence of electric field lines is greater in the sensor centre than at the periphery leading to greater measurement integrity in the centre (5). An iterative non-linear reconstruction algorithm has also been applied to 3D-ECT measurement data and compared with traditional linear back projection; suffice to say the non-linear algorithm showed significantly improved results (16).

The academic group responsible for the previously mentioned 'limited region tomography' (7, 8) also investigated using a novel ECT sensor coupled with a resolution analysis method to determine the sensitivity of image error and resolution to electrode and sensor design (17). This study provides a step change in the protocols used to design 3D-ECT sensors and certainly gives greater impetus to the argument for increased use of this technology in industry.

Given the usefulness of the information gathered, there is potential for 3D-ECT to be integrated into engineering processes (18). However, so far there

have been few works published using a commercial instrument. 2D-ECT has so far been applied to a wide range of engineering processes, however the majority of published work has been carried out on academic instruments in either single or dual plane configuration. Few ECT instruments are commercially available and the capability for 3D image reconstruction amongst these is very low, the main reason being a lack of image accuracy which is problematic for real-world industrial applications. Indeed the implementation of a reconstruction package into a useable graphical user interface (GUI) has only recently been published (19).

The present paper addresses this need by applying commercially available 3D-ECT technology to image a series of mobile phantoms. The phantom used is a simple cylinder-in-tube setup that demonstrates both a moving object and a hard boundary, in this case the interface between polyethylene and air. A methodology, initially developed on 2D-ECT images, that improves image accuracy using optimised binary thresholds is then applied to the 3D-ECT tomograms.

2 Materials and Methods for 3D-ECT Imaging

The objectives of this work were to determine the usefulness of ECT as an online measurement tool for interface detection within a 3D sensing zone and to investigate the capability of a commercially available ECT instrument to deliver 3D images of a transient system including an evolving interface.

2.1 Cylinder-in-Tube Phantom Configuration

In order to show the development of a hard interface in the radial plane moving axially through the sensor a series of phantom experiments were designed. Phantoms are objects of known dimensions that simulate a desired process or system. A triple plane ECT sensor was used comprising a polyether ether ketone (PEEK) cylinder of inner diameter 156 mm with three planes of eight electrodes implanted to the outside of the wall and encased in stainless steel. A cylinder-in-tube PE phantom was used to simulate the interface. The PE tube had diameter 142 mm with an annular core of diameter 30 mm, tube wall thickness 62 mm and length 300 mm. The PE cylinder was 30 mm in diameter and 300 mm long with a flanged base having a diameter of 160 mm. The schematics for these phantoms are given in **Figure 1**.

The small cylinder (**Figure 1(b)**) and sensor were raised above the large tube (**Figure 1(a)**) and imaged at penetration intervals of $^1/_8$ of the length of the small cylinder. Once the whole of the large tube had been removed, the sensor was imaging just the small cylinder with a large air gap between the sensor wall
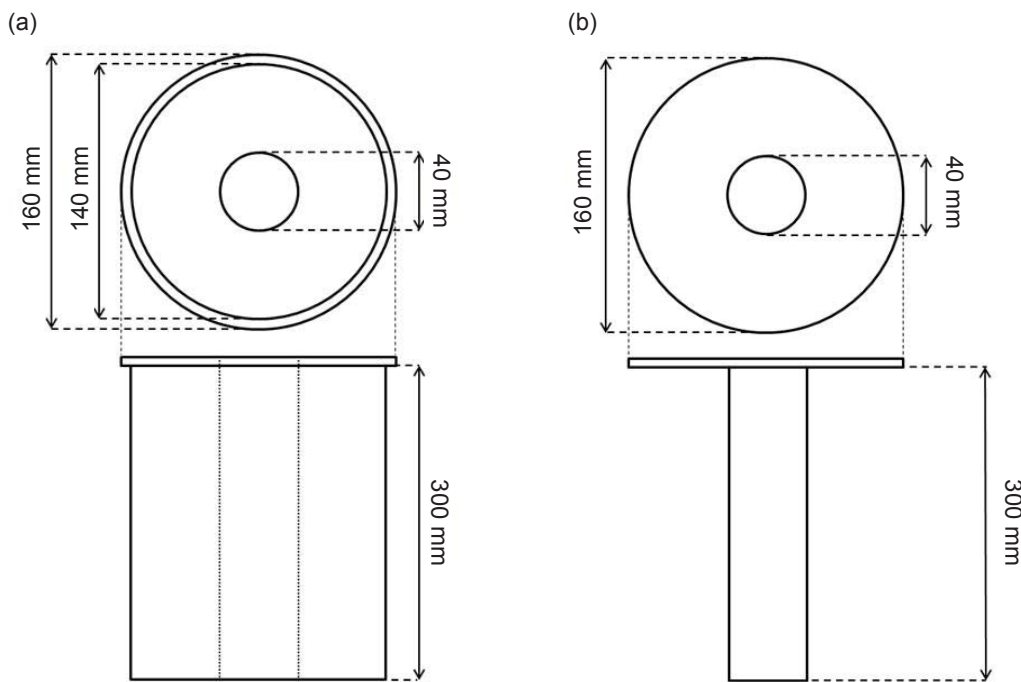

Fig. 1. Schematics for cylinder-in-tube phantom experiments: (a) thick-walled PE tube showing annulus; (b) PE cylinder with flange base

and the phantom. The $^1/_8$ penetration intervals were measured and marked onto the polyethylene cylinder shown in **Figure 2(b)**.

Figure 2(a) shows the large tube housed within the PEEK-lined ECT sensor. There is an air gap of 1 mm between the PE large tube and the wall of the sensor. As this is present during the sensor calibration it has no impact on the reconstructed ECT data. The $^1/_8$ intervals of the length of the small cylinder at which the large tube was imaged are shown in **Figure 2(b)** as markings on the small cylinder.

2.2 ECT Setup and Configuration

The ECT instrument used for this work was an Industrial Tomography Systems (ITS) m3c 24 input channel unit. Individual electrodes were connected from the sensor to the instrument ports using Bayonet Neill-Concelman (BNC) cables. The first step in processing of electrical tomography data is normalisation of the capacitance data according to Equation (iv):

$$C_n = \frac{C - C_l}{C_h - C_l} \qquad \text{(iv)}$$

Where C_n and C are the normalised and measured capacitance values respectively, and C_h and C_l are capacitance values from the high permittivity and low permittivity reference frames respectively. The reference frames are taken prior to measurement and for both experimental series the conditions for these are given in **Table I**.

The low permittivity reference frame is taken prior to the high permittivity reference frame and once both are acquired process data can be recorded. The phantom experiment was imaged for 30 frames at each of the large tube holding intervals thus building a series of images of penetration depth of the small cylinder.

(a) Co-axial cable housing, ECT sensor, Pipe annulus, PEEK pipe

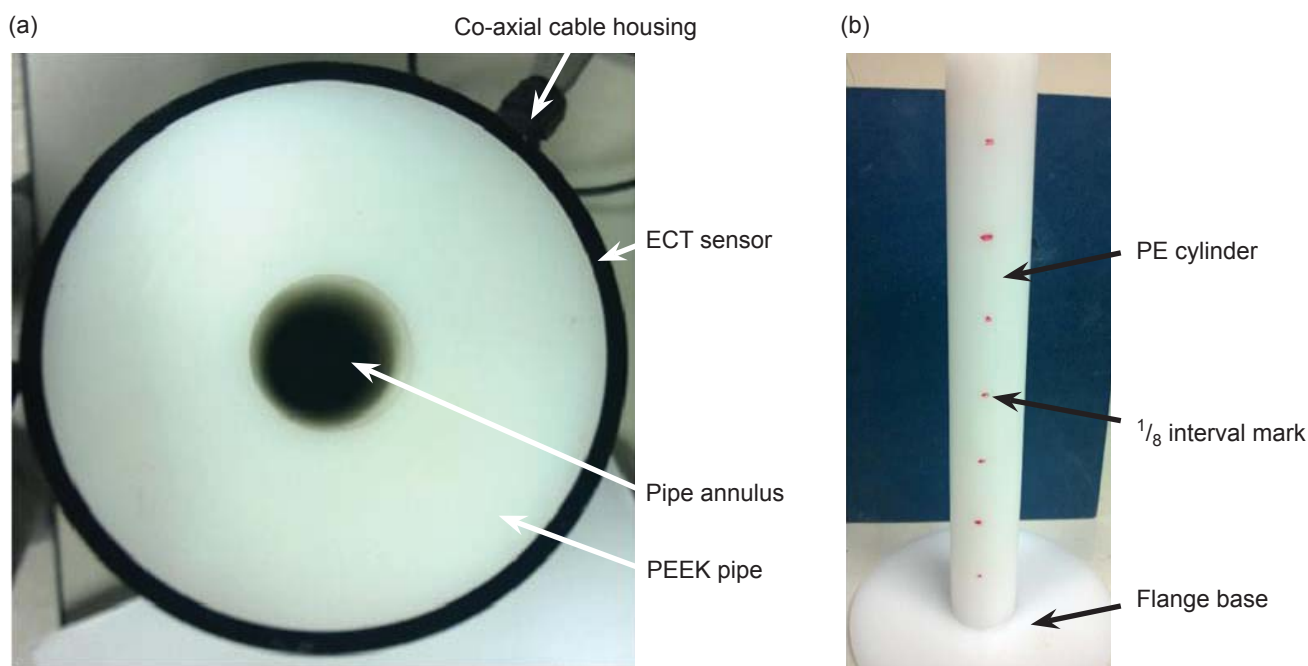(b) PE cylinder, $^1/_8$ interval mark, Flange base

Fig. 2. Individual components of cylinder-in-tube phantom: (a) thick-walled PE tube within PEEK-lined ECT sensor; (b) 40 mm diameter PE cylinder with flanged base

Table I High and Low Permittivity Reference Frames: Material Properties for Both Phantom and Drying Bed Experimental Series				
Experimental series	**High permittivity reference frame[a]**		**Low permittivity reference frame[a]**	
	material	ε_r	**material**	ε_r
Phantom	PE	2.2–2.4	Air	1.5

[a] ε_r = Relative permittivity

A reconstruction algorithm is required to calculate the spatially resolved material data from electrical boundary measurements. In commercial ECT equipment there has previously been just one algorithm available to use: the LBP algorithm. This is a single-step algorithm that requires less computing power due to its simplicity and delivers fast results; however the reconstructed images are inaccurate (5). It assumes a linear relationship between the capacitance and permittivity vectors as given in Equation (v):

$$g = S^T \lambda \qquad \text{(v)}$$

where g is the normalised permittivity vector, λ is the normalised capacitance vector and S^T is a linear approximation to the inverse of the sensitivity matrix, S (20). This equation is solved by discretisation across a pixel grid containing 1024 pixels that is reduced to 812 pixels as the corners are filleted for circular images. Although LBP has several drawbacks, it is the most commonly used method in industry and is therefore used for reconstructing data within this paper.

2.3 3D-ECT Tomogram Image Processing

A true 3D-ECT measurement acquires charge data in both the radial and axial direction for each stimulus, yielding an output of a 3D tomogram composed of $32 \times 32 \times 32$ voxels (corresponding to pixels in 3D space). Each voxel represents a volume portion within the sensor and is assigned a value in the interval between 0 and 1. In order to identify the geometrical shape placed in the sensor, a binary gating method is applied. This method, widely applied in MRI and in 2D-ECT, consists of dividing the tomogram into a number of zones equivalent to the number of phases. In this study one zone represents the volume occupied by the phantom and the second is composed of the surrounding gas phase (5). Once the image has been thresholded it is possible to compare it with a previously built reference to evaluate the image error. The advantage of using phantoms is that their exact geometry is known and therefore a digitalised reference image as basis for comparison for error analysis is accurate and simple to construct.

The data processing methods applied in the refinement of 2D images have been applied also to the 3D-ECT tomogram analysis. The objective of the gating method is to find the optimum threshold value to allow generation of the binary matrix that describes the object with the minimum error. A reference image has been created to allow the comparison between the reconstructed tomograms and the real object, this image is given in **Figure 3**.

The PbP approach, defined as voxel-by-voxel in 3D tomography, compares the corresponding voxels in the reconstructed and in the theoretical images (**Figure 3**) and is described by the same equation as PbP analysis (Equation (i)). The areal approach (Equations (ii) and (iii)) is extended to the third dimension by evaluating the volume occupied by the phantom in the image, Equation (vi):

$$V_{image} = V_C \frac{\sum \mu_{image}}{N} \bigg|_{\mu_{image<t}} \qquad \text{(vi)}$$

where V_{image} is the volume of the image and V_C is the total volume of the sensor chamber. The volumetric error is calculated by evaluating the ratio of the difference between the volumes of the imaged and the real object and the volume of the real object, Equation (vii):

$$e_v = \frac{\left| V_{image} - V_{phantom} \right|}{V_{phantom}} \qquad \text{(vii)}$$

where e_v is the image error calculated using the volumetric-areal approach and $V_{phanton}$ is the volume of the phantom.
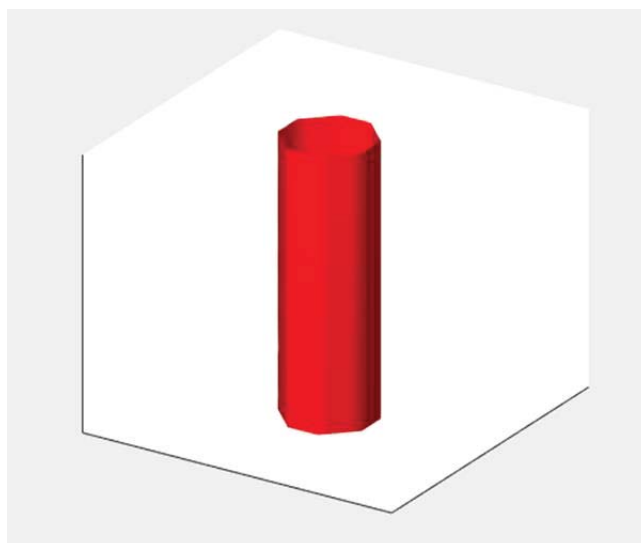

Fig. 3. Pixelated reference image of fully withdrawn PE cylinder from PE tube for comparison in voxel-by-voxel analysis

3 Results and Discussion

The phantom experiments use PE, with a low relative permittivity, to simulate an interface so the 3D-ECT reconstruction can be trialled using the basic LBP algorithm to ascertain its efficacy before application to high di-electric media. Therefore these experiments are used solely to examine whether 3D-ECT is capable of monitoring an interface.

3.1 3D-ECT Reconstruction using LBP

The ECT three-plane sensor is attached to the flanged base of the small cylinder therefore the phantom is defined as the large tube being inserted into the sensor

with the PE/air interface being the top of the PE large tube. The tomograms are shown in **Figure 4**.

The images displayed in **Figure 4** are cross-section tomograms whereby the electrode measurements from the three planes of uniform electrodes are reconstructed and subsequently discretised to give 16 image planes. In pseudo-3D tomography this form of image is strongly discouraged as the lack of axial inter-electrode capacitance data nullifies any assumptions required to use an inter-plane interpolation approach. This is not the case in 3D-ECT as inter-electrode capacitances on different planes have been measured. **Figure 4(a)** shows the system at full immersion, that is to say the small cylinder is fully
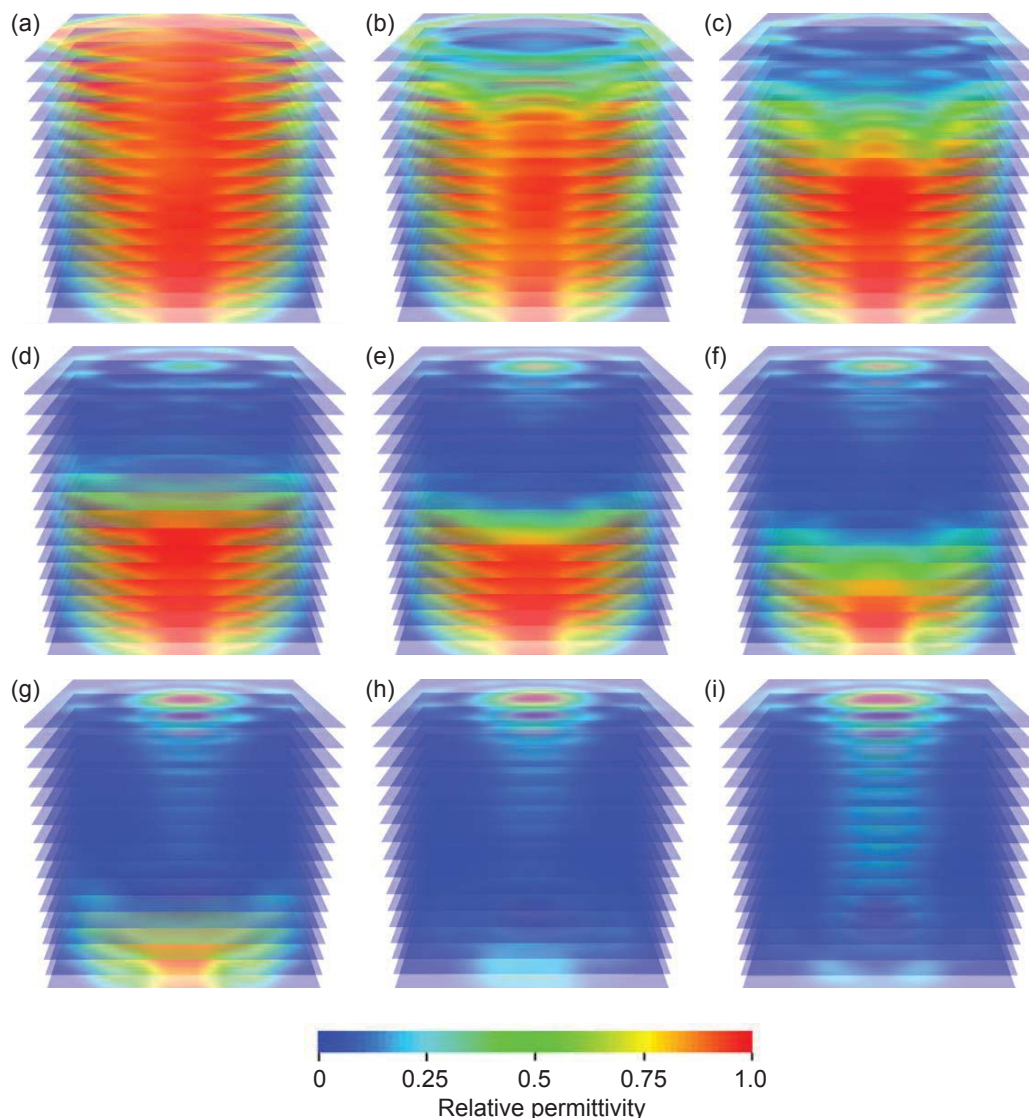

Fig. 4. Cross-section sliced 3D tomograms of cylinder-in-tube phantom experiment: (a) fully immersed phantom; (b) $^7/_8$ immersed; (c) $^3/_4$ immersed; (d) $^5/_8$ immersed; (e) $^1/_2$ immersed; (f) $^3/_8$ immersed; (g) $^1/_4$ immersed; (h) $^1/_8$ immersed; (i) fully withdrawn

immersed in the large tube. The colour scheme of these charts indicate low permittivity regions as being blue and high permittivity regions as being red, however the corners of the square pixel grid are included in these reconstructed images and coloured blue. These pixels are present in all the cross-section slice tomograms, however they are not representative of the circular sensor (in 2D-ECT these are typically removed from the image) and are therefore excised from all analyses.

The large tube is withdrawn from the ECT sensor at intervals of $^1/_8$ penetration. It can be seen in **Figure 4(b)** that a reduction in the mean conductivity across the electrode plane occurs and continues through the other images within **Figure 4** as the phantom moves through the sensor. The small cylinder is present inside the cylinder at all times even as the large tube is removed from the sensing zone. The first evidence of the presence of the small cylinder phantom is in **Figure 4(e)** where a series of voxels in the centre of the top cross-section planes of the 3D image register an increase in the permittivity. Moving from **Figure 4(e)** to **Figure 4(h)** it is clear this area of high permittivity spreads down the 3D tomograms in this series. This has to be attributed to the presence of the small cylinder in the centre of the sensor, however the shape of the high permittivity region is not clear which is unsurprising given that the air gap between the cylinder and the sensor wall is 51 mm. The air gap affects the linearity assumption used in the sensitivity matrix. However, it is surprising that the small cylinder is affecting the inter-electrode electric field given the size of this air gap. The images given in **Figure 4** have been smoothed to a high degree that gives the impression of soft edges in the process.

To better represent the interface between low and high permittivity phases iso-surface plots of the same experiment are presented in **Figure 5**. Iso-surface plots were calculated from volumetric data (given in **Figure 4**) and represent constant scalar data within a scalar 3D distribution. In the case of the phantom experiments this is represented as the interface between PE and air. Initially, in **Figure 5(a)**, the sensor was at the equivalent of a high permittivity reference frame as the large tube was fully immersed in the sensor. The four rectangular regions at the sensor boundary are image artefacts and enclose the high permittivity region; they are able to be excised from the images but have been retained to give clarity as regards to the phase distribution. As the large PE tube was removed from the sensor the interface

was clearly shown to progress down the sensor. **Figure 5(d)** shows the presence of the small cylinder at the top of the image, indicating that although the large tube was $^5/_8$ immersed in the sensor and the small cylinder occupied the centre of the void behind the interface, it was not clearly detected by the sensor. When the large tube reached $^1/_4$ immersed (**Figure 5(g)**) the small tube was imaged as a rounded cone and the interface of the large tube and air was clearly present at the bottom of the sensor. The imaged shape of the small cylinder was consistent from **Figure 5(e)** to **Figure 5(h)** and was only imaged as a cylinder once the large tube was fully removed from the sensor in **Figure 5(i)**. This result is symptomatic of a number of limitations of the technique in its current state: the limit of the software to drive a maximum of three planes; the reconstruction algorithm when imaging hard boundaries; and the low permittivity ratio between the two phases (σ_{air} = 1, σ_{PE} = 2.3). ECT therefore images the permittivity difference between phases by keeping this difference high and the ability of the instrument to detect a hard boundary theoretically increases.

3.2 Binary Image Refinement of 3D-ECT Tomograms

Following on from the evaluation of accuracy of 2D-ECT tomograms, a similar error analysis has been applied to the cylinder-in-tube experiment. The reference image for the voxel-by-voxel analysis was shown in **Figure 3**. The voxel values are extracted from the tomographic data and processed using MATLAB® (MathWorks® Inc). The voxel-by-voxel error and the volumetric error are calculated for several values in the interval between 0.2 and 0.7 in order to evaluate the optimal value in terms of minimum error.

As shown in **Figure 6** in both cases it is possible to reach very low errors and the optimum threshold value does not change substantially. It is 0.501 according to the voxel-by-voxel analysis (**Figure 6(a)**) and 0.547 by applying the volumetric analysis (**Figure 6(b)**). This characteristic is an important sign of the robustness of the reconstruction and leads to the conclusion that the results do not change substantially if the threshold value is fixed for either error analysis methodology. In fact, using the voxel-by-voxel method to compare the errors when choosing the threshold value at the minimum of **Figure 6(a)** and **Figure 6(b)**, gives values of 0.0306 and 0.0316 respectively. This confirms the strength of the volumetric analysis which unlike the voxel-by-voxel
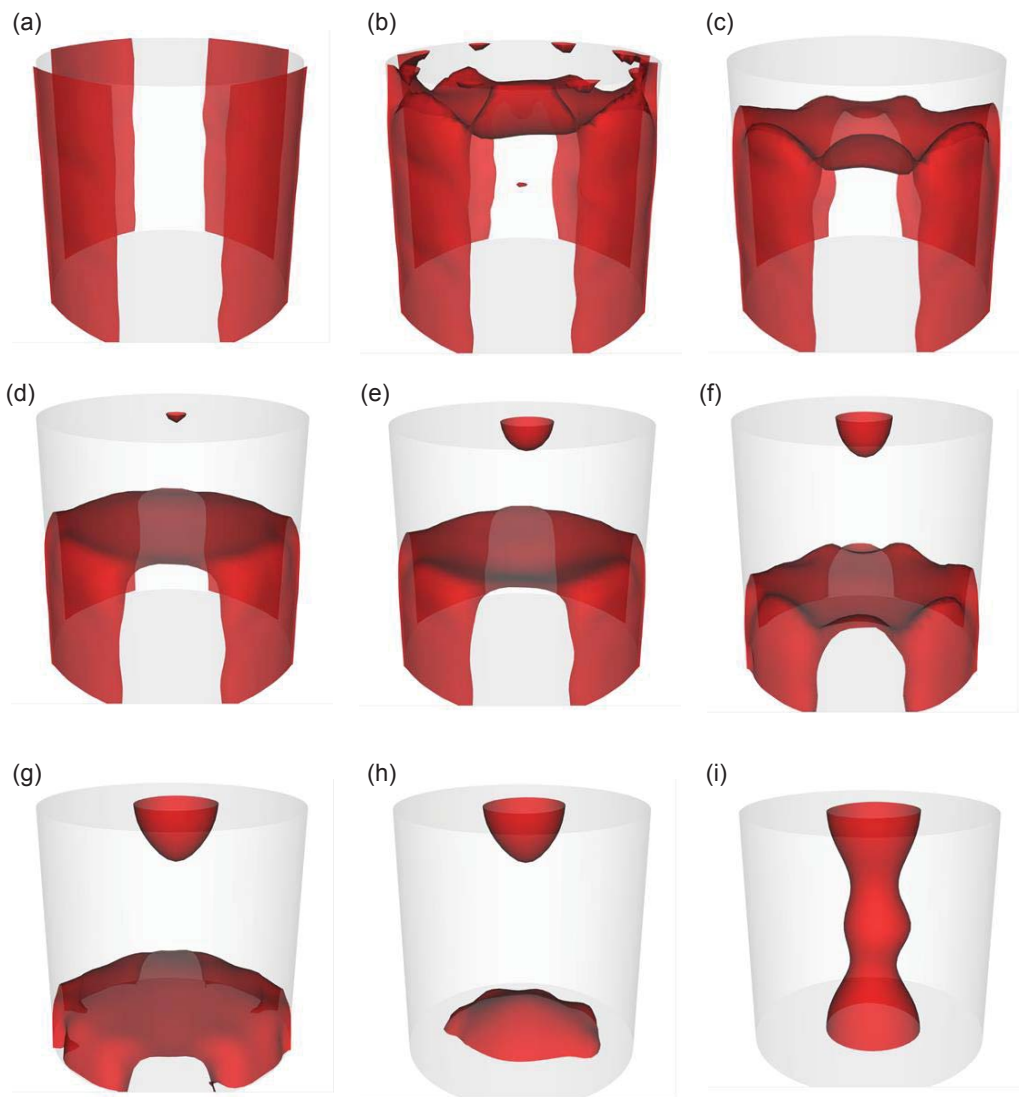
Fig. 5. Iso-surface plots of PE cylinder-in-tube phantoms: (a) fully immersed large tube phantom; (b) $^7/_8$ immersed; (c) $^3/_4$ immersed; (d) $^5/_8$ immersed; (e) $^1/_2$ immersed; (f) $^3/_8$ immersed; (g) $^1/_4$ immersed; (h) $^1/_8$ immersed; (i) fully withdrawn
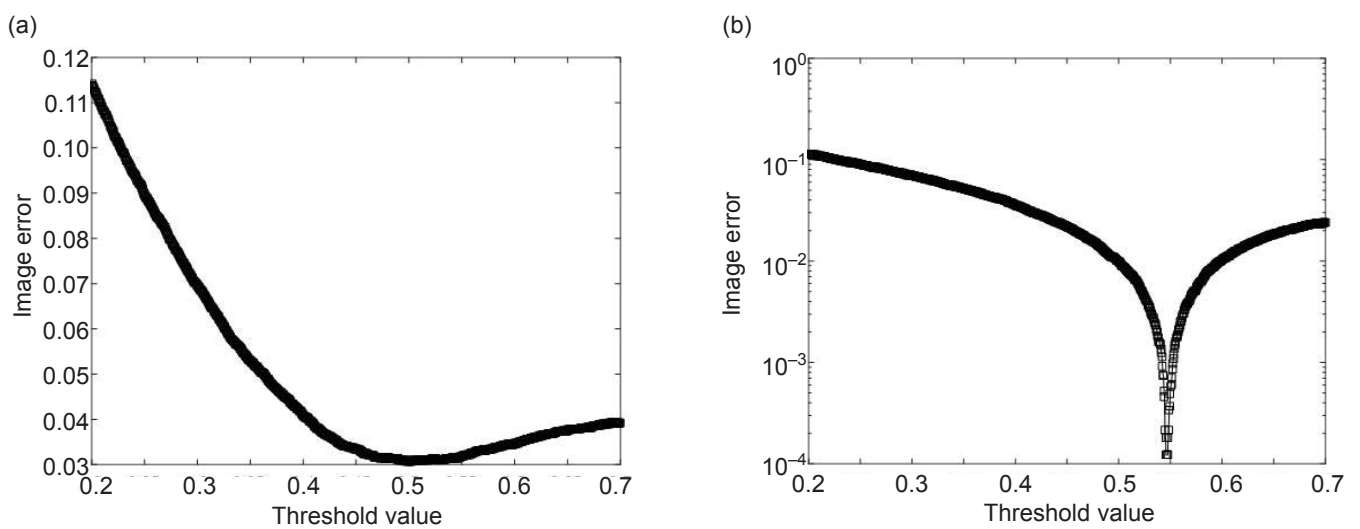

Fig. 6. Binary sensitivity to thresholds of 3D-ECT tomograms of polymethyl methacrylate (PMMA) cylinders: (a) voxel-by-voxel error analysis; (b) volumetric analysis

analysis does not need precise geometric information relative to the position of the phantom or objects within the sensor.

In **Figure 7** the iso-surface plots display the reconstructed interface between the phantom and the gas phase using the threshold value suggested by the voxel-by-voxel analysis (**Figure 7(a)**) and the volumetric analysis (**Figure 7(b)**).

The obtained images from both analyses are very similar with both unable to display a geometric cylindrical shape, a limitation of the spatial resolution provided by single-step reconstruction algorithms. The permittivity difference between the air and PE is approximately two thereby reducing the SNR of the measurement and leading to lower image accuracy. The data post-processing improves the image accuracy as the images in **Figure 7** represent the cylindrical phantom more closely than those in **Figure 5(i)**. To reduce image error the two available options with the current ECT instrumentation are to use an alternative reconstruction algorithm or to improve the phase permittivity difference.

4 Conclusions

This paper examines recent innovations in the field of 3D electrical capacitance tomography and the application to 3D-ECT of previously used 2D-ECT post-processing methods that improve tomogram accuracy of imaged geometric phantoms. Firstly, development work of the data processing techniques applied to 2D-ECT was examined and shown to be effective, then using a similar phantom system the 3D-ECT method was used to acquire

3D tomograms and a similar analysis was adopted. It has been shown that commercially available ECT equipment has the capability to image a mobile object and yield information on the location of a hard boundary in 3D space.

The images were optimised using a previously published method whereby the threshold value of the image was optimised by correlation with image error. A voxel-by-voxel approach to calculating image error was compared with a volumetric approach demonstrating the robustness of the latter as it does not require precise geometric information to provide improved tomographic accuracy. The image accuracy of ECT is a function of the spatial resolution that is dependent upon both the software (reconstruction algorithm and data processing) and hardware (electrodes and data acquisition system (DAS)) used in the measurement. When these are improved the quality of the reconstructed images improves thereby making this method more applicable to chemical processes.
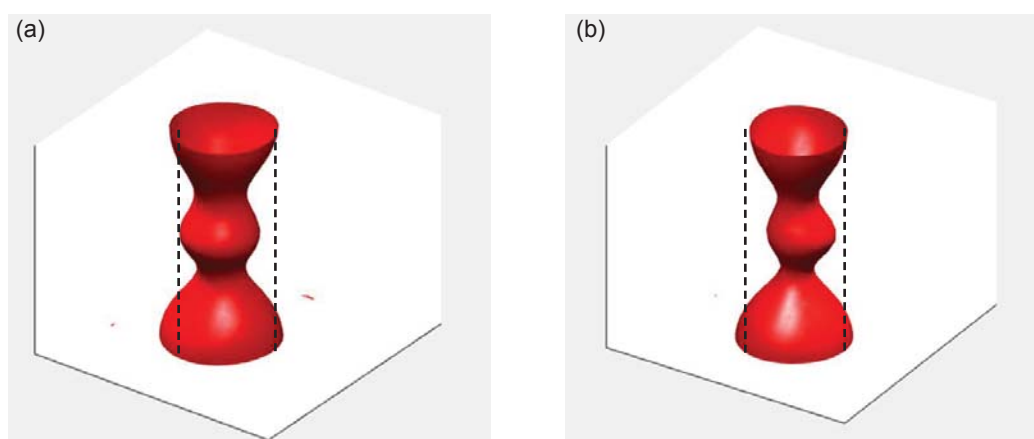
5 Acknowledgements

Fig. 7. 3D-ECT iso-surface plots with applied optimal threshold value and dashed lines showing object location: (a) voxel-by-voxel threshold value = 0.501; (b) volumetric threshold value = 0.547

References

1. L. Peng, C. Mou, D. Yao, B. Zhang and D. Xiao, *Flow Meas. Instrum.,* 2005, **16**, (2–3), 169

2. H. Xu, G. Yang and S. Wang, 'Effect of Axial Guard Electrodes on Sensing Field of Capacitance Tomographic Sensor', in "Proceedings of 1st World Congress on Industrial Process Tomography", Buxton, UK, 14th–17th April, 1999, pp. 348–352

3. A. J. Jaworski and G. T. Bolton, *Meas. Sci. Technol.,* 2000, **11**, (6), 743

4. M. Hamidipour and F. Larachi, *Chem. Eng. J.,* 2010, **165**, (1), 310

5. P. J. Clark, A. N. Tsoligkas, M. J. H. Simmons, P. T. Robbins and E. H. Stitt, *Meas. Sci. Technol.,* 2016, **27**, (2), 025401

6. P. J. Clark, A. N. Tsoligkas, M. J. H. Simmons, S. Blackburn and H. Stitt, 'Detection of Phase and Other Sharp Boundaries using Electrical Capacitance Tomography' in "Proceedings of 7th World Congress on Industrial Process Tomography", Krakow, Poland, 2nd–5th September, 2013, pp. 799–808

7. E. Al Hosani, M. Zhang and M. Soleimani, *IEEE Sens. J.,* 2015, **15**, (11), 6089

8. M. Evangelidis, L. Ma and M. Soleimani, 'Pipeline Inspection Using High Resolution Electrical Capacitance Tomography', in 'Proceedings of 7th World Congress on Industrial Process Tomography', Krakow, Poland, 2nd–5th September, 2013, pp. 556

9. R. Wajman, R. Banasiak, L. Mazurkiewicz, T. Dyakowski and D. Sankowski, *Meas. Sci. Technol.,* 2006, **17**, (8), 2113

10. V. Rimpiläinen, L. M. Heikkinen and M. Vauhkonen, *Chem. Eng. Sci.,* 2012, **75**, 220

11. W. Warsito and L.-S. Fan, *Chem. Eng. Proc.: Proc. Intens.,* 2003, **42**, (8–9), 663

12. W. Warsito and L.-S. Fan, 'Development of 3-Dimensional Electrical Capacitance Tomography Based on Neural Network Multi-Criterion Optimization Image Reconstruction', in "Proceedings of 3rd World Congress on Industrial Process Tomography", Banff, Canada, 2nd–5th September, 2003, pp. 391–396

13. W. Warsito and L.-S. Fan, *Chem. Eng. Sci.,* 2005, **60**, (22), 6073

14. T. C. Chandrasekera, A. Wang, D. J. Holland, Q. Marashdeh, M. Pore, F. Wang, A. J. Sederman, L. S. Fan, L. F. Gladden and J. S. Dennis, *Powder Technol.,* 2012, **227**, 86

15. M. Soleimani, C. N. Mitchell, R. Banasiak, R. Wajman and A. Adler, *Prog. Electromagn. Res.,* 2009, **90**, 171

16. R. Banasiak, R. Wajman, D. Sankowski and M. Soleimani, *Prog. Electromagn. Res.,* 2010, **100**, 219

17. Z. Ye, H. Y. Wei and M. Soleimani, *Measurement,* 2015, **61**, 270

18. P. J. Clark, N. P. Ramskill, M. J. Simmons, A. York, L. F. Gladden and E. H. Stitt, 'Validation of Electrical Capacitance Tomography Drying Measurements using Magnetic Resonance Imaging', in 7th International Symposium on Process Tomography, Dresden, Germany, 1st–3rd September, 2015

19. K. Wei, C. Qiu, M. Soleimani and K. Primrose, *Flow Meas. Instrum.,* 2015, **46**, (Part B), 292

20. W. Q. Yang and L. Peng, *Meas. Sci. Technol.,* 2003, **14**, (1), R1

The Authors

Peter Clark is a Process Engineer working at Johnson Matthey within Platinum Group Metal Services. Peter obtained a MEng (Hons) in Chemical Engineering at the University of Birmingham, UK, and then undertook an Engineering Doctorate within the Johnson Matthey Technology Centre, Chilton, UK, where he applied advanced characterisation tools, including but not exclusively process tomography, to a range of chemical engineering applications.

Giuseppe Forte is an engineering doctoral student at the University of Birmingham, whose research project is jointly funded by the Engineering and Physical Sciences Research Council (EPSRC) and Johnson Matthey. His current research, based at Johnson Matthey Technology Centre, Chilton, concerns the development of on-process measurement techniques for monitoring formulated products. Before joining his current position, he obtained his MEng in Chemical Engineering from the University of Pisa, Italy. His interests and expertise focus on industrial electrical tomography, acoustic spectroscopy and image processing.

Professor Mark Simmons is Professor of Fluid Mechanics and Head of the School of Chemical Engineering at the University of Birmingham. His research interests encompass how flows can be utilised or exploited in processes which are used to manufacture complex multiphase products, including catalysts, foods and fast moving consumer goods (e.g. shampoos, detergents). He has applied his expertise in flow measurement, sensing and rheology in a variety of projects funded by EPSRC, Biotechnology and Biological Sciences Research Council (BBSRC) and industry: notably Johnson Matthey, Unilever and Rolls-Royce. Professor Simmons is a Fellow of the Institution of Chemical Engineers, has published over 100 peer-reviewed papers and has graduated over 32 PhD and EngD students.

E. Hugh Stitt is a Scientific Consultant at Johnson Matthey Technology Centre, Chilton, UK. He is a Visiting Professor at the University of Birmingham, UK, and at Queen's University Belfast; Fellow of the Institution of Chemical Engineers and a Fellow of the Royal Academy of Engineering. He has 25 years of industrial research experience across a variety of themes related to catalytic reaction engineering and catalysts with over 100 refereed publications.